Computer Modeling in Engineering & Sciences
DOI:10.32604/cmes.2020.09934
Article

Investigation into Spatter Particles and Their Effect on the Formation Quality During Selective Laser Melting Processes

Zhiqiang Wang[1], Xuede Wang[1], Xin Zhou[1,*], Guangzhao Ye[2], Xing Cheng[1,3] and Peiyu Zhang[1]

[1]Science and Technology on Plasma Dynamics Laboratory, Air Force Engineering University, Xi'an, 710038, China
[2]School of Mechanical and Automotive Engineering, South China University of Technology, Guangzhou, 510640, China
[3]Aero-Space Engine & Smart Manufacturing Institute, Xi'an, 710038, China
*Corresponding Author: Xin Zhou. Email: dr_zhouxin@126.com
Received: 03 February 2020; Accepted: 25 March 2020

Abstract: During the selective laser melting process, a high-energy laser beam acts on the powder, a molten pool is rapidly generated and the characteristic parameters are constantly changing. Among them, temperature is one of the important parameters in the forming process. Due to the generation of splash particles, there will be defects in the microstructure, which will seriously affect the formation quality of the prepared parts. Therefore, it is necessary to study the relationships between the splash behavior, molten pool characteristics and product quality. The finite element simulation of the transient temperature field was performed by ANSYS software. Time-series images at different frame rates were obtained with a high-speed camera, and the dynamic process of splashing was observed. Using IN718 alloy powder, the influence of the laser energy density on the light intensity of the molten pool was studied. The appearance of splash particles and the deviation of the powder chemical elements caused by the splash were analyzed. The results show that the transient temperature field with drastic change is easy to cause spatter, which is consistent with the experimental results. There are large differences in the splash at different shooting frame rates. Increasing the frame rate can allow the observation of details such as the shape, size and number of splash particles, which is beneficial for studying the process of splash formation. At the moment when the splash occurs, the light intensity of the molten pool always first increases and then decreases, depending on the energy input. The higher the energy input is, the more intense the light intensity of the molten pool and the higher the peak interval distribution. Compared with fresh powder, the contents of Al and Ti in powder reused 5 times were reduced by 0.15% and 0.02%, respectively. The increases of these two elements in the splash were 16.18% and 29.62%, respectively, and the content of Nb even exceeded the standard range. When the energy density decreased from 229.17 J/mm^3 to 130.95 J/mm^3, the relative density of the part increased from 91.82% to 99.83%. This shows that reducing the energy input can reduce the splash to suppress the generation of defects, along with the weakening of the overall light intensity of the molten pool. These results can provide a basis for feature extraction of the molten pool, which is of great significance for real-time monitoring and online control in manufacturing processes and ensuring product quality.

Keywords: Selective laser melting; temperature field simulation; spatter behavior; molten pool characteristics; defect

1 Introduction

Selective laser melting (SLM) is an additive manufacturing technology based on the principle of "discrete-stacking", which lays powder layer by layer and melts metal materials layer by layer to build three-dimensional solid parts [1–4]. Because of its great flexibility in terms of the shapes of raw materials and processed parts, it is considered to have broad development prospects and has attracted widespread attention [5–8]. In addition, the SLM process overcomes the limitations of traditional processing methods [9] and can produce parts with high molding accuracy, good surface quality integrity, compact structures, and excellent mechanical properties [2,10,11]. The method has been widely used in the aerospace, medical, marine and automotive fields [12–14]. However, the high-energy laser beam acts on the powder, and the powder absorbs the heat to rapidly melt to form a molten pool, and then the molten pool is rapidly cooled, which adversely affects the stability of the molten pool. In addition, the interaction between the laser and powder involves a complicated thermal conduction process, usually accompanied by the generation of spatter [15]. Spatter particles will contaminate the fresh powder, cause defects in the internal microstructure of the part, reduce the part densification, and seriously affect the part manufacturing performance and quality [16]. Therefore, the study of splash behavior is very important both to control the intensity of the splash to eliminate defects and to obtain parts that meet actual needs.

The research of SLM is mainly focused on the process parameters, microstructures, properties and simulations of SLM parts made of various materials. Wang et al. [17–19] found that changing the energy input by controlling regional process parameters can improve the manufacturing quality and processing efficiency of products. In addition, they found that the surface roughness of SLM parts could be improved by laser re-melting method. Song et al. [20] and Bai et al. [21] studied the mechanical properties of CoCrMo alloy and maraging steel 300 SLM manufacturing parts, respectively. Heat treatment was found to increase the elongation and tensile properties of the manufactured parts. Chen et al. [22] found that the external magnetic field can make the surface of the molten pool smoother in the simulation of the surface deformation control of AlSi10Mg material. Jia et al. [23] found that the high temperature performance of IN718 superalloy can be improved by optimizing the laser process and its control method.

Splash particles are one of the main sources of defect generation in the SLM formation process, and some researchers have carried out studies on splash behavior. Zhang et al. [24–26] considered that the generation of splash was caused by the action of metal vapor and plasma on the molten pool; Low et al. [27–29] studied the mechanism of splash generation during laser drilling, the effect of process parameters on the splash particles, and the development of a composite coating that can reduce splashing. Liu et al. [30] studied the type and formation mechanism of 316 stainless steel during the SLM process and found that the laser energy input has a significant effect on the size of the splash particles, that the scattering state and spray height also have a significant effect, and that the splash seriously reduces the mechanical properties of the molded part. Wang et al. [31,32] studied the effects of splash and the number of powder reuse cycles on the tensile properties of CoCr-01 and CoCrW alloys, respectively. It was found that these will adversely affect the formation quality of the part due to the inclusions generated by the spatter and the increase in the number of times the powder is used. Simonelli et al. [33] studied the effect of the oxidation behavior on the composition of the splash particles in the SLM process and found that the splash particles have an impact on the environment, the oxygen content is very sensitive, and the reused powder elemental composition changes greatly compared to fresh powder. Andani et al. [34,35] developed a computer image analysis frame to assess the size, number, and distribution of splash particles. It was found that unfused defects caused by splashes are detrimental to the mechanical

properties of SLM parts, and changing the laser scanning speed has a greater impact on sputtering formation in comparison with the energy input.

In the process of laser melting powder, it is very difficult to observe and record the transient temperature field experimentally to study the thermophysical mechanism. Using numerical simulation is an important way to solve this problem and further understand the forming mechanism of SLM. Simultaneously, there are many complicated thermophysical processes such as thermal radiation, thermal convection and thermal conduction, so it is difficult to deeply understand the formation mechanism of the splash. The splash particles are mixed with fresh powder to form inclusions, which can also cause internal defects in parts and affect the quality of product manufacturing. So far, there have been few reports on the light intensity of the molten pool in the SLM process and its correlation with splash behavior. Therefore, this article uses IN718 alloy powder as a material to simulate the transient temperature field during the SLM process, study the formation mechanism of splash, quantify the light intensity of the molten pool under different energy inputs, and comparatively study the deviation of the powder chemical composition caused by splash. This research can provide a basis for the extraction of parameters such as the temperature of the molten pool, the area of the molten pool, the length of the molten pool, and the width of the molten pool. It is of great significance for achieving real-time monitoring and online control in the manufacturing process and ensuring product quality.

2 Conditions and Methods of Simulation and Experiment

2.1 Establishment of Physical Model in SLM Process

The thermal physical model in SLM process is shown in Fig. 1. The thermophysical mechanism is very complex, mainly including the radiation between the laser and the powder bed, the heat conduction between the metal substrate and the powder particles, and the thermal convection/thermal radiation between the surface of the powder bed and the surrounding environment.

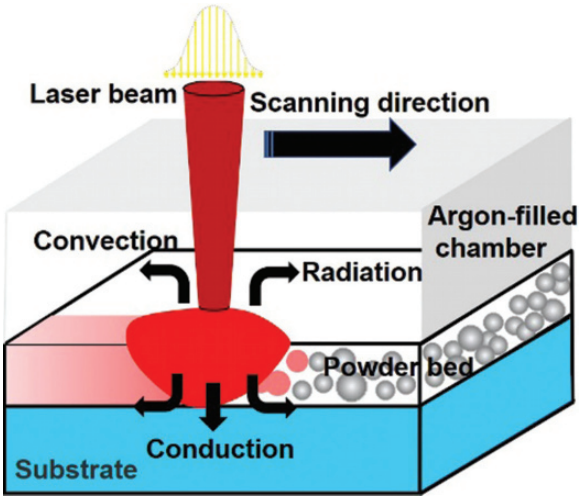

Figure 1: Thermophysical model of SLM process

2.1.1 Governing Equation

SLM temperature field analysis is a transient heat conduction problem, which satisfies the 3D transient heat conduction equation:

$$\rho c\frac{\partial T}{\partial t}=\frac{\partial}{\partial x}(k_x\frac{\partial T}{\partial x})+\frac{\partial}{\partial y}(k_y\frac{\partial T}{\partial y})+\frac{\partial}{\partial z}(k_z\frac{\partial T}{\partial z})+Q \tag{1}$$

where ρ is the density of the material, c is the specific heat capacity of the material, T is the material's transient temperature, t is the time, k_x, k_y, and k_z are the heat conduction rates of the material in the x, y, and z directions, respectively, and Q is the heat generated per volume.

Before the heat source is loaded, assuming the ambient temperature is 20°C, the initial conditions of the temperature field can be expressed as:

$$T(x,y,z)_{t=0}=T_0 \tag{2}$$

During the SLM forming process, there is thermal convection and thermal radiation between the surface of the powder bed and the surrounding environment, so the boundary conditions of the temperature field can be expressed as:

$$k\frac{\partial T}{\partial n}-q+h(T-T_0)+\sigma\varepsilon(T^4-{T_0}^4)=0 \tag{3}$$

where T_0 represents the ambient temperature, q represents the heat flux, h represents the thermal convection coefficient, σ represents the Stefan-Boltzmann constant, which is approximately 5.67×10^{-8} W/(m^2·K^4), and ε represents the heat radiation coefficient.

2.1.2 Loading of Mobile Heat Sources

The ANSYS parametric design language (APDL) was used to load the Gaussian heat source, and the laser beam meets the energy distribution:

$$q=\frac{2AP}{\pi R^2}\exp(-\frac{2r^2}{R^2}) \tag{4}$$

where A is the laser absorptivity of the material, P is the laser power, R is the laser spot radius, and r is the distance from a point on the powder bed to the center of the spot.

2.1.3 Treatment of Latent Heat of Phase Transition

Phase transformation occurs during the melting and solidification of the powder, accompanied by the release and absorption of latent heat. In this paper, enthalpy method is used to define latent heat:

$$H=\int \rho c(T)dT \tag{5}$$

where H is the enthalpy, ρ is the density of the material, c is the specific heat capacity of the material, and T is the transient temperature of the material.

2.1.4 Physical Parameters of Materials

The effective thermal conductivity of the powder bed is an important parameter for temperature field simulation and can be expressed as:

$$k_{\mathrm{pr}}=k_{\mathrm{sd}}(1-\varphi) \tag{6}$$

where k_{pr} and k_{sd} are the effective thermal conductivity of the powder and solid, respectively, φ is the porosity of the powder bed, and its mathematical expression is as follows:

$$\varphi = \frac{\rho_{sd} - \rho_{pr}}{\rho_{sd}} \tag{7}$$

where ρ_{pr} and ρ_{sd} are the density of powder and solid, respectively. The powder selected in this paper is IN718 alloy with a melting temperature range of 1260°C–1320°C. The physical properties of the material and the finite element simulation parameters of the SLM process are shown in Tabs. 1 [36] and 2.

Table 1: Thermal-physical parameters of IN718 [36]

T(°C)	20	100	200	400	600	800	1300
k_{sd}(W·m^{-1}·°C^{-1})	10	12	14	17	20	26	31
c(J·kg^{-1}·°C^{-1})	362	378	400	412	460	544	583

Table 2: Finite element simulation parameters in SLM process

Parameter	Value
Absorptivity, A	0.35
Ambient temperature, T_0 (°C)	20
Laser power, P (W)	55
Scan speed, SS (mm·s^{-1})	200
Layer thickness, LT (μm)	20
Laser spot radius, R (μm)	100

2.1.5 Establishment of Finite Element Model

The finite element model established in this paper is shown in Fig. 2. The powder bed material is IN718 powder with dimensions of 1.4 mm × 1 mm × 0.02 mm and the powder layer thickness is 0.02 mm. The substrate is 45 # steel with a size of 2 mm × 2 mm × 0.15 mm. The powder layer is meshed by ANSYS Soild70 hexahedron eight-node thermal element, and the substrate is selected by tetrahedron element for free meshing. Considering the number of meshes and calculation efficiency, the laser spot radius used in this simulation is 100 μm, which is larger than the actual spot radius. The purpose is mainly to simulate the process of laser melting powder. Three points of P1-P3 were set on the scanning path by single-channel scanning to study the temperature distribution at different positions (Point P1 at the starting position, Point P2 at the center and Point P3 at the end position).

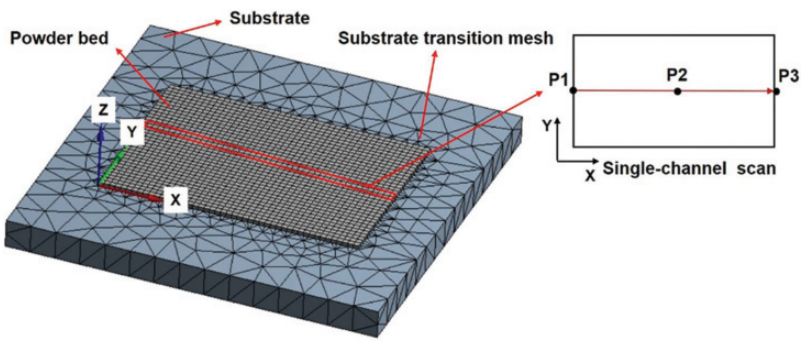

Figure 2: Finite element model and single-channel scanning method

2.2 Experimental Equipment and Materials

The experiment was performed on the SLM machine Di-Metal 50 and high-speed photography equipment, as shown in Fig. 3. The SLM machine consists of an optical system, scanning system, fresh air protection system, path-planning control software system, etc. The infrared ytterbium fiber laser has a peak power of 75 W, with a TEM00 Gaussian energy density distribution. The working mode of the laser is a continuous wave with a wavelength of 1060–1070 nm. The size of the building envelope is 50 mm × 50 mm × 50 mm. The focusing optical system uses a lens with a focal length of 100 mm and can produce an ultrasmall focusing spot of approximately 20 μm. The scanning system is equipped with a high-precision scanning galvanometer. The f-theta lens is used to guide the X-axis and Y-axis laser beams. The maximum scanning speed is 7 m/s. Before the experiment, the laser power and beam diameter of the laser are calibrated, and the laser start delay parameters of the galvanometer are set. The laser on/off delay parameters of the galvanometer are optimized, thus the fluctuation of the laser processing parameters is reduced [37]. A double-cylinder unidirectional powder supply is used, and the layer thickness is 0.02 mm–0.1 mm. During the SLM molding process, high-purity argon gas is introduced as a protective gas, and fresh argon gas is introduced under the optical lens to form a protective gas layer, which can isolate the burning materials during the powder-melting process to prevent them from adhering to the lens and ensure the absolute laser output accuracy. Because the oxygen content is critical during SLM processing, the oxygen content must be less than 0.01% during the forming process. The main technical parameters of Di-Metal 50 are shown in Tab. 3. A high-speed camera (Phantom v2512) was used to capture the dynamic splashing process of metal droplets during SLM forming of the IN718 alloy at different frame rates.

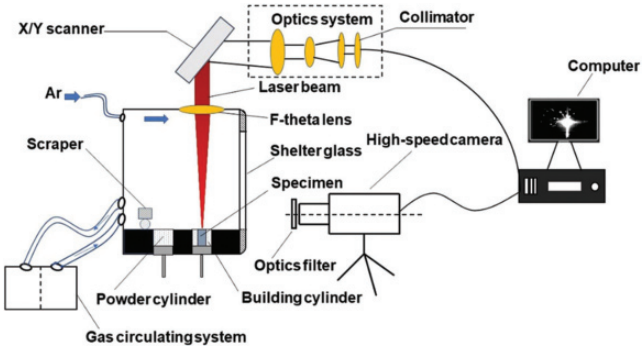

Figure 3: Schematic diagram of the SLM machine and high-speed photography equipment

Table 3: Main technical parameters of the DiMetal-50

Item	Value	Item	Value
Max laser power	75 W	Max scanning speed	7 m/s
Wavelength	1060–1070 nm	Building envelop	50 mm × 50 mm × 50 mm
Focus length	100 mm	Min focusing spot	20 μm
Layer thickness	0.02–0.1 mm	Hatch spacing	60–85 μm

The material used in this study is IN718 nickel-based gas atomized spherical superalloy powder from Oerlikon Metco, USA. Figs. 4(a) and 4(b) depict the morphology and the size distribution (wt.%) of the powder particles, respectively. The powder particle size is in the range of 24.085 μm to 46.333 μm, as

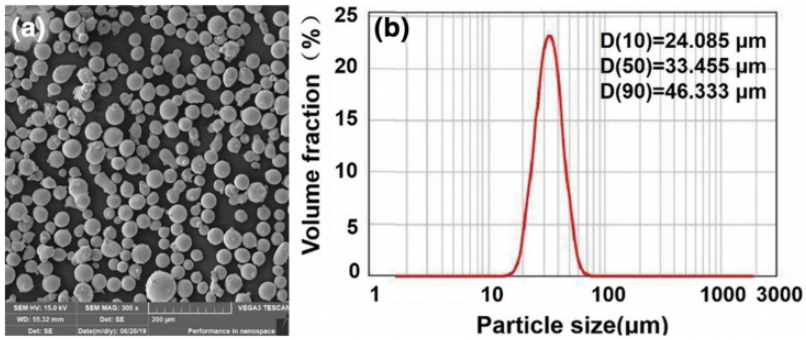

Figure 4: IN718 powder: (a) SEM morphology, and (b) particle size distribution

measured by a HHTA0014 laser particle-size analyzer. To mitigate the oxidation of the molten pool, the high-purity Ar gas in the building chamber is controlled at approximately 1–2.0 Lh^{-1}.

2.3 Experimental Methods

The SLM processing parameters are shown in Tab. 4, and the energy input is defined as Eq. (8) [38].

$$E = \frac{P}{SS \cdot HS \cdot LT} \tag{8}$$

where P, SS, HS, and LT are the laser power (W), laser scanning speed (mm/s), hatch spacing (mm), and layer thickness (mm), respectively. The scanning speed was set as 200 mm/s, 250 mm/s, 300 mm/s, and 350 mm/s, and the four different scanning speeds were selected to study the impact of the scanning speed on spatter during SLM (HS = 60 μm, LT = 20 μm, and P = 55 W).

Table 4: Process parameters and energy input in this study

Sample	Laser power (W)	Scanning speed (mm/s)	Energy input (J/mm^3)
1	55	200	229.17
2	55	250	183.33
3	55	300	152.78
4	55	350	130.95

All samples were installed in epoxy resin, ground to 2,000 mesh on SiC sandpaper, and then polished with diamond suspensions of 6 μm, 2.5 μm, and 1 μm, respectively. Microscopic analysis was performed using a digital video microscope (HIROX, RH-8800). A scanning electron microscope and laser particle-size analyzer were used to observe the morphology and particle size distribution of the sputtered particles, and EDS spectrum analysis was performed. The test method was based on EPA 6010D-2018. The chemical compositions of the fresh powder, powder and splash after repeated use were analyzed by Inductively Coupled Plasma Optical Emission Spectrometer (ICP-OES), which can continuously and quickly measure multiple elements with a wavelength range of 160–800 nm. The light intensity of the molten pool was monitored with the help of ImageJ software, through which the changes in the light intensity of the molten pool during the dynamic process of splashing were studied, and the understanding of the mechanism of splash formation was deepened. Finally, the internal defects of the samples were compared to verify the effect of the sputtering particles on the internal defects of the part.

3 Results and Discussion

3.1 Analysis of Transient Temperature Field in SLM Process

When the laser heat source radiates to the surface of the powder bed, the powder absorbs a part of the laser energy, and the remaining laser energy generates thermal radiation with the surrounding environment. A micro-melt pool is formed when the energy absorbed by the powder exceeds its own melting point. Temperature distribution is an important reference to reflect the process of laser melting powder. Fig. 5 shows the temperature nephogram of the overall model, as well as the upper surface and longitudinal cross-section morphology of temperature nephogram of P1-P3. Under the action of Gaussian heat source, a series of oval isotherms were formed on the upper surface of the molten pool. The isotherm at the front end of the molten pool is denser than that at the rear end. The reason is that the powder at the rear end of the molten pool is solidified, while the front end of the molten pool is still in a powder state. Furthermore, the powder has lower thermal conductivity than solids, and the heat cannot be effectively conducted to cause a larger temperature gradient, so the isotherm at the front end of the molten pool is denser. In addition, the temperature of the center points of the temperature nephogram of P1, P2, and P3 gradually increased to 1051.5°C, 1955.7°C, and 2060.7°C, respectively. This is due to the accumulation of heat with the increase of the scanning time.

The temperature probe in ANSYS software is used to monitor the maximum temperature of the whole scanning process and the temperature of point P1-P3, as shown in Fig. 6. It can be seen from Fig. 6(a) that the maximum temperature in the single-channel scanning process is 1331.7°C at 0.21 ms, exceeding the melting point of the powder. The maximum temperature increases continuously from 0.21 ms to 7 ms, up to 2101.8°C. In addition, the maximum temperature is almost above the melting point with the maximum difference value up to 841.8°C, which is easy to make the molten pool oscillate and cause splashing. The maximum temperature at point P1-P3 is 1136.6°C, 2011.8°C and 2101.8°C, respectively. The regularity of temperature variation is as follows: when the laser beam is close to the point, the temperature increases rapidly, then reaches the maximum temperature in a very short time. Finally, the temperature decreases rapidly when the laser is far away from the point.

3.2 Formation Mechanism and Observation of Spatter Particles

As shown in Fig. 7, when a laser beam of a certain energy density irradiates the powder material, a molten pool is formed with dazzling bright light, the surface of the material quickly evaporates, and a metal vapor mass is formed above the molten pool. Pressure acts on the molten pool, and on the one hand, it causes steam depressions in the molten pool, while on the other hand, it causes some molten material to be sprayed out to form a metal liquid column [39]. At the same time, due to the Marangoni convection effect, the metal melt flows from the hot bottom of the molten pool depression to the low-temperature side of the rear of the molten pool in the opposite direction of the scanning speed [32]. For the IN718 alloy, the surface tension temperature coefficient $d\sigma/dT$ is negative [40], and the surface tension decreases as the temperature of the molten pool increases. Driven by recoil pressure and Marangoni force, when the local kinetic energy of the melt exceeds the surface tension, a low-viscosity liquid is ejected, and the droplet spatter is formed. In addition, the unmelted powders around the molten pool are dispersed due to the influence of metal vapor. However, the size and shape of the powder are basically unchanged [30], and this type of spatter is called powder spatter. Furthermore, during the dynamic process of spatter formation, the light intensity of the molten pool can be related to the degree of spatter, which would be helpful for understanding the mechanism of spatter formation.

Fig. 8 shows the splash behavior at different shooting frame rates, this is consistent with the result of the finite element analysis of the transient temperature field. The fixed laser power is 55 W, the scanning speed is 200 mm/s, and the shooting frame rates are 100 FPS, 300 FPS, and 1000 FPS, where FPS (Frames Per

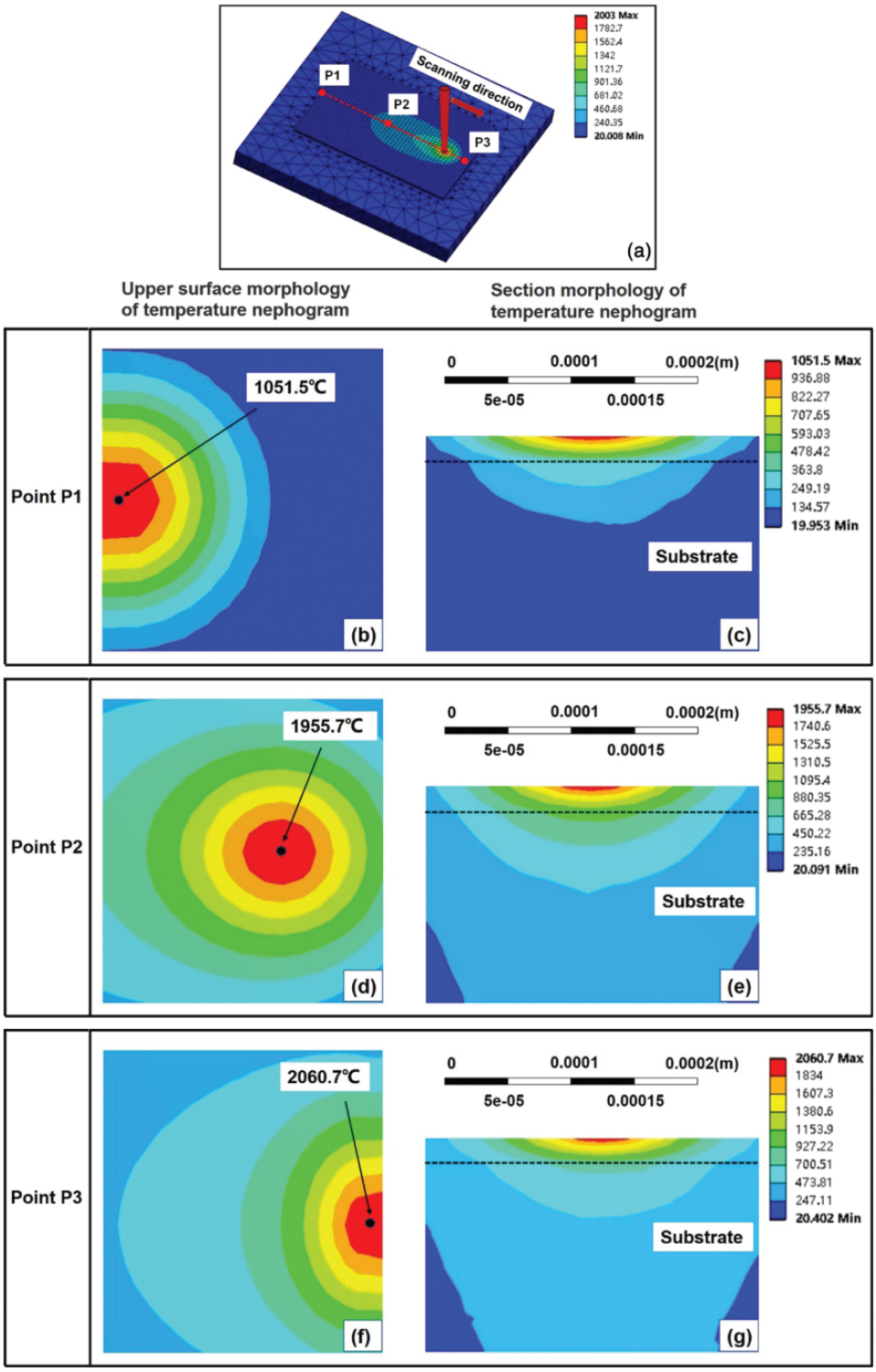

Figure 5: Upper surface and longitudinal cross-section morphology of temperature nephogram: (a) temperature nephogram of the overall model, (b)-(c) upper surface and longitudinal cross-section morphology of temperature nephogram of P1, (d)-(e) upper surface and longitudinal cross-section morphology of temperature nephogram of P2, and (f)-(g) upper surface and longitudinal cross-section morphology of temperature nephogram of P3

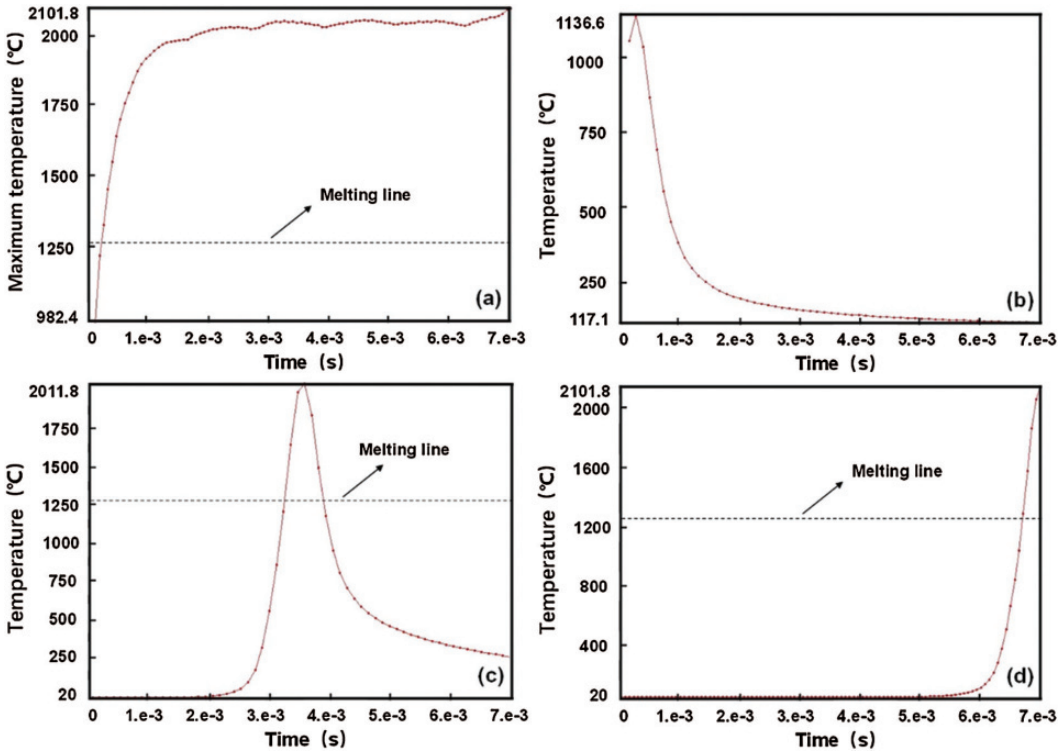

Figure 6: The regularity of temperature changing with time in the single-channel scanning process: (a) the regularity of the maximum temperature changing with time, and (b)-(d) the regularity of the temperature changing with time of P1, P2 and P3, respectively

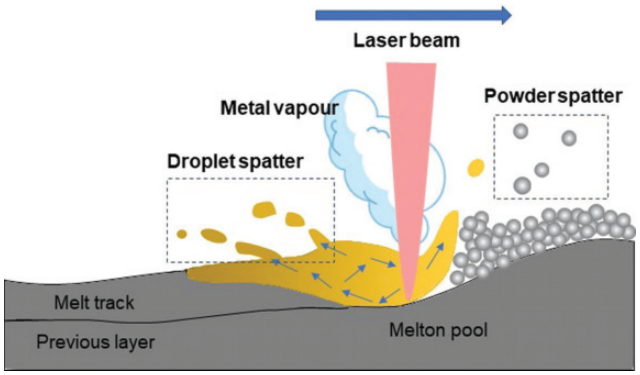

Figure 7: The mechanism of spatter formation under the action of metal vapor related to the light intensity of the molten pool

Second) refers to the number of images taken per second by a high-speed camera. The sputtering behavior was found to vary with the shooting frame rate.

As shown in Fig. 8(a), when the shooting frame rate is 100 FPS, dazzling bright light from the molten pool can be observed, and the bright splash trail is very obvious. The shape and size of the splash particles cannot be observed, which is not conducive to studying the splash behavior dynamic process.

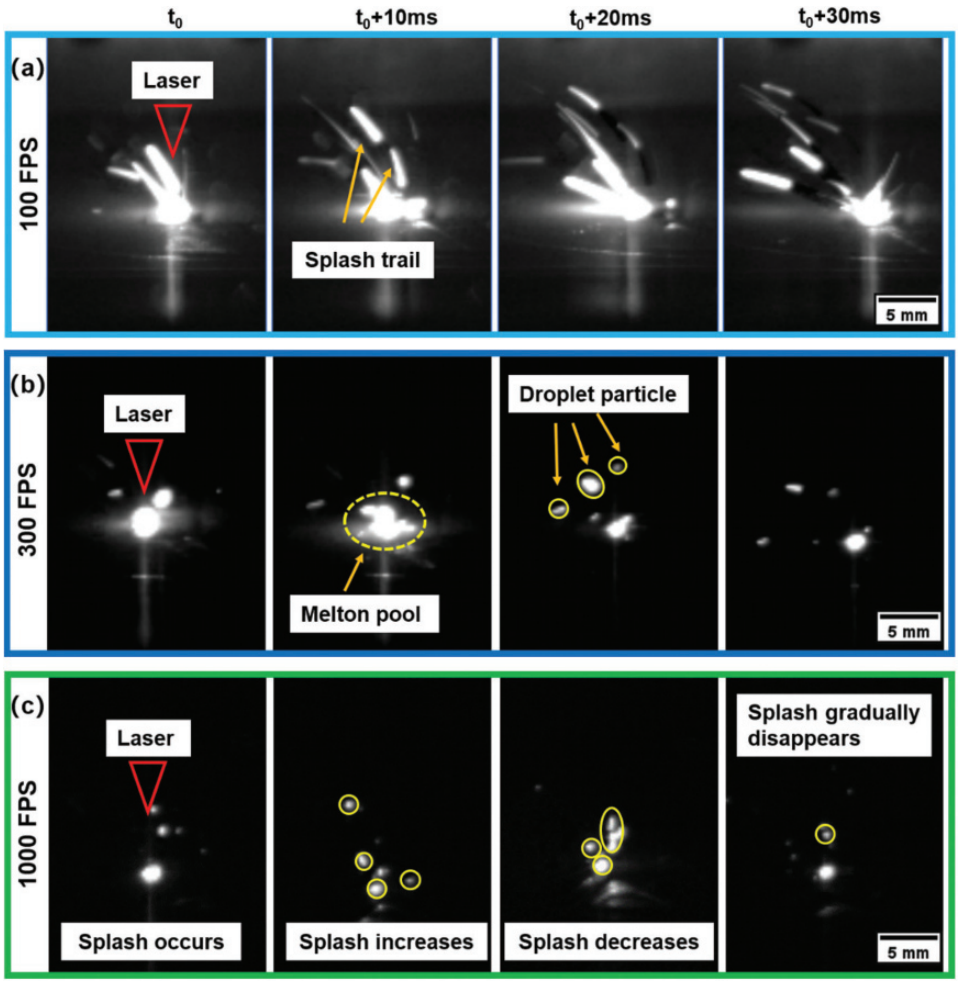

Figure 8: Comparison of time-series spatter images at different shooting frame rates: (a) spatter images of resolution 640 × 480 and a frame rate of 100 FPS, (b) spatter images of resolution 640 × 480 and a frame rate of 300 FPS, and (c) spatter images of resolution 640 × 480 and a frame rate of 1000 FPS

When the shooting frame rate is 300 FPS, the detailed process of the splash behavior is displayed, and the shape and size of the molten pool and splash droplets are easy to observe, as shown in Fig. 8(b). This is caused by the increase in the shooting frame rate. The light in molten pool is brighter at the beginning of the splash, and the brightness decreases after the sputtered particles are ejected. During the spattering process, it was found that in the nonlaser radiation area, the metal splash separated into many small droplets [20].

When the shooting frame rate is increased to 1000 FPS, as shown in Fig. 8(c), it depicts the dynamic process of splashing from generation to gradual disappearance. During this process, the light intensity of the molten pool changes continuously, the droplet particles become more obvious, and the number of splash particles first increases and then decreases. Furthermore, the results demonstrate that the evolution of the number of splash particles under laser irradiation can be divided into three stages, as follows: the stage of splash increasing, from t_0 to t_0 + 10 ms; the stage of splash decreasing, from t_0 + 10 ms to t_0 + 20 ms; the stage of splash gradually disappearing, from t_0 + 20 ms to t_0 + 30 ms.

During the dynamic process of spatter formation, constant changes in the light intensity of the molten pool can be observed. Fig. 9 shows the molten pool images and light intensity trends during a complete

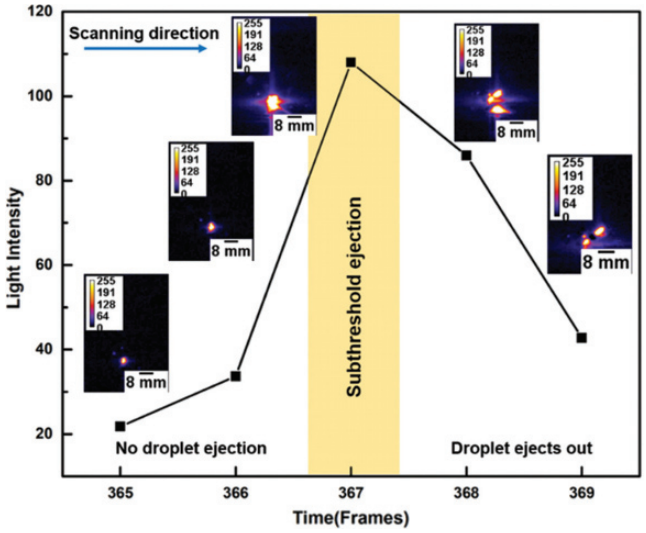

Figure 9: Light intensity and droplet spattering state during the spatter generation process at a scanning speed of 200 mm/s. At the moment of the splash, the light intensity of the molten pool first increases and then decreases, reaching a peak value at the subthreshold ejection

splash formation process at a scanning speed of 200 mm/s and a shooting frame rate of 1000 FPS. The intensity changes of the light intensity of the molten pool were measured in the 1000-frame shooting time series images. It was found that when there was no droplet sputtering, the light intensity of the molten pool was low. The light intensity gradually increased as the splash gradually formed, with the light intensity increasing from 21.77 to 108.02. The light intensity reached a maximum value during the sputtering quasi-steady state. After the droplets were sputtered out, the light intensity decreased from a maximum value of 108.02 to 42.76.

3.3 Correlation Between the Light Intensity of the Molten Pool and the Spatter Behavior

To further study the changes of the light intensity of the molten pool during the generation of splash, the inherent relationship between the light intensity and the splash was established. With a shooting frame rate of 1000 FPS and other conditions unchanged, the scanning speed was changed to monitor the molten pool within 1 s. The light intensity changes are shown in Figs. 10(a)–10(d), with the scanning speeds of 200 mm/s, 250 mm/s, 300 mm/s, and 350 mm/s. In Fig. 10(a), the energy density is 229.17 J/mm^3, and the light intensity of the molten pool changes most drastically. In the 367th frame, the light intensity is as high as 108.02, and the peak value is mainly distributed within the range of 60 to 80. When the energy density is 183.33 J/mm ^{3}, the light intensity of the molten pool is large, with the light intensity as high as 68.00 in the 113th frame, and the peak values are mainly distributed within the range of 40–60, as shown in Fig. 10(b). In Fig. 10(c), the energy density is reduced to 152.78 J/mm^3, and the light intensity of the molten pool is weakened. The peak interval is reduced to within the range of 30–50. The maximum light intensity is 57.92 at 591 frames. At a minimum energy density of 130.95 J/mm^3, the light intensity of the molten pool is different from those in the three cases discussed above. It is the weakest overall. Most of the peaks are concentrated in the 20 to 30 range, as is shown in Fig. 10(d). At 766 frames, the maximum light intensity is only 41.27. The intensity of the droplet splash will tend to increase as the energy input increases [30]. This study found that the light intensity of the molten pool is closely related to the energy input. The larger the input, the stronger is the light intensity. This reflects the change law of the splash intensity. The larger the light intensity, the more intense is the change, and the larger the splash intensity, the more intense is the change.

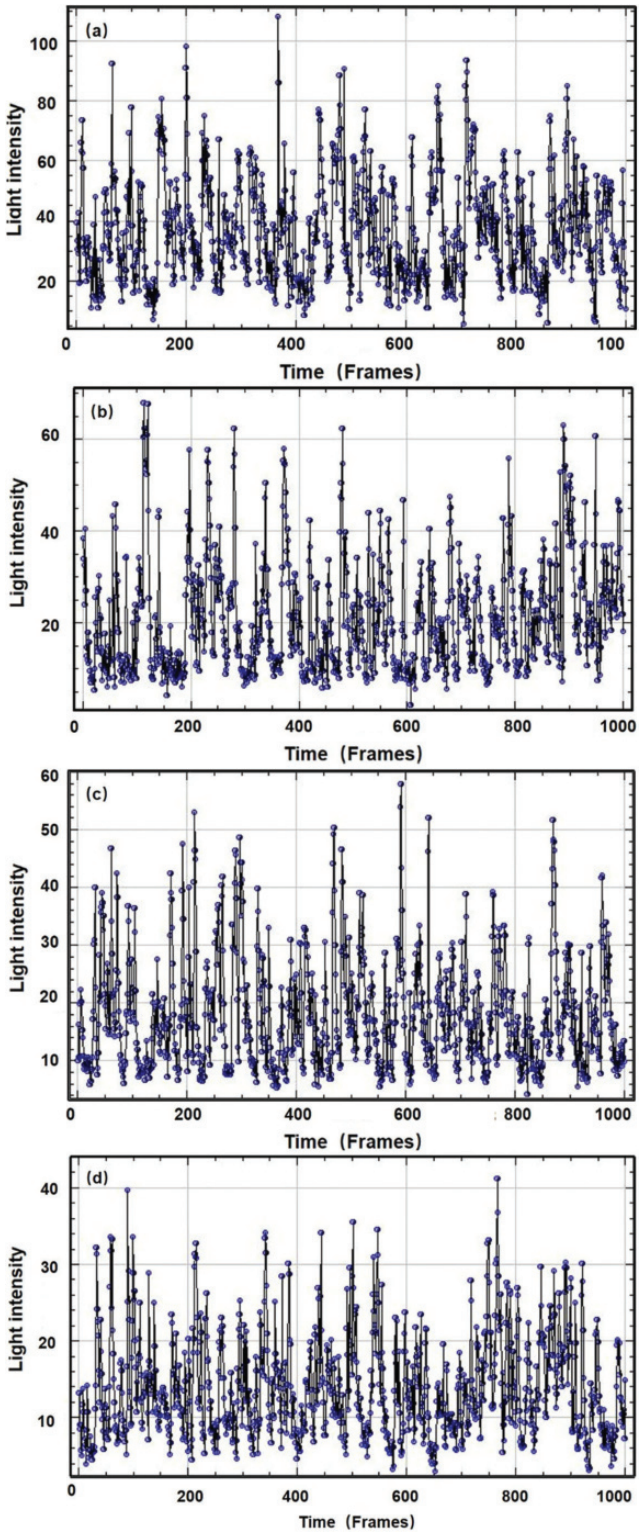

Figure 10: Variation of the light intensity of the molten pool at different scanning speeds with the frame rate of 1000 FPS: (a) laser on the 20 μm-thickness powder with a scanning speed of 200 mm/s, (b) laser on the 20 μm-thickness powder with a scanning speed of 250 mm/s, (c) laser on the 20 μm-thickness powder with a scanning speed of 300 mm/s, and (d) laser on the 20 μm-thickness powder with a scanning speed of 350 mm/s

3.4 Analysis of the Morphology and Elemental Composition of the Spatter Particles

Fig. 11 shows a micromorphology image of fresh powder and splash particles. As shown in Fig. 11(a), the morphology of the fresh powder has a high sphericity, and the surfaces of the powder particles are smooth. Splash particles can be divided into three types: ellipsoidal splash, coarse spherical splash and irregular splash [19]. Figs. 11(b)–11(d) show coarse spherical splashes, but the morphologies of the three are different, and the amount of unmelted powder attached to the surface of the splash particles gradually increases. It is generally believed that under the effect of recoil pressure, the molten pool sprays particles to higher and longer distances [38]. Particles with a larger splash distance can cool in the Ar for a longer time or even completely solidify, producing lower amounts of adherent powder with smooth surfaces (ellipsoidal splash). This shows that the unmelted powder attached to the spatter particles increases with the decrease of the dwell time. When the metal liquid column is ejected from the molten pool, the surface tension gradually shrinks it into spherical droplets to minimize the surface energy [41]. The irregular shapes of the splash particles shown in Figs. 11(e)–11(f) indicate a short splash distance, which cannot form a sphere in time; thus, the unspheroidized irregular spatter with many fine powder particles attached is formed.

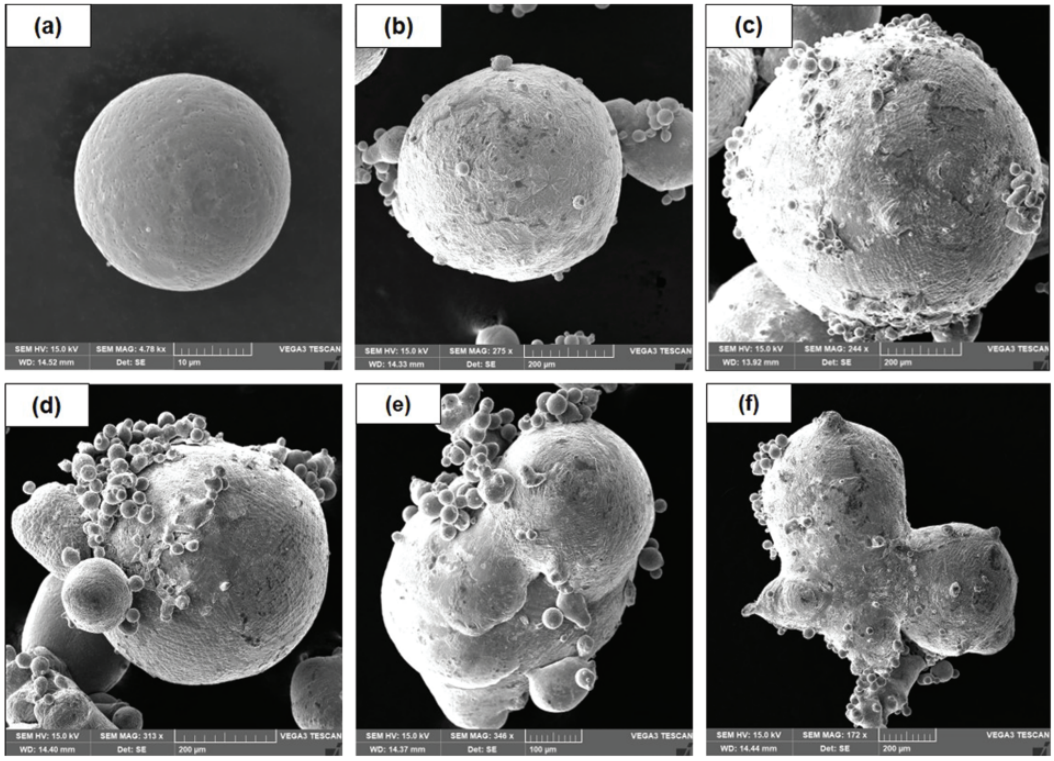

Figure 11: SEM images of fresh powder and spatter particles: (a) morphology of fresh powder, (b)–(d) morphology of coarse spherical splash with different amounts of powder attached, and (e)–(f) appearance of irregular splashes that fail to spheroidize in time

Tab. 5 shows the reference of the chemical composition of the standard IN718 powder provided by the manufacturer. Figs. 12(a)–12(b) illustrate the results of an energy scattering spectrometer (EDS) measurement of powder and splash particles after use. Compared with the fresh powder, it can be clearly found that the content of Al and Ti in the powder reused 5 times is reduced by 0.15% and 0.02%, respectively, and these two elements in the splash increase by 16.18% and 29.62%. This is because the melting point of molten Al is only 660°C, making it easily splash out of the molten pool. The melting

Table 5: Chemical composition of IN718 powder

Element	Cr	Fe	Mo	Nb	Co	Al	Ti	Ni
Content (wt. %)	20.20	19.20	3.00	5.01	0.09	0.52	0.85	Bal.

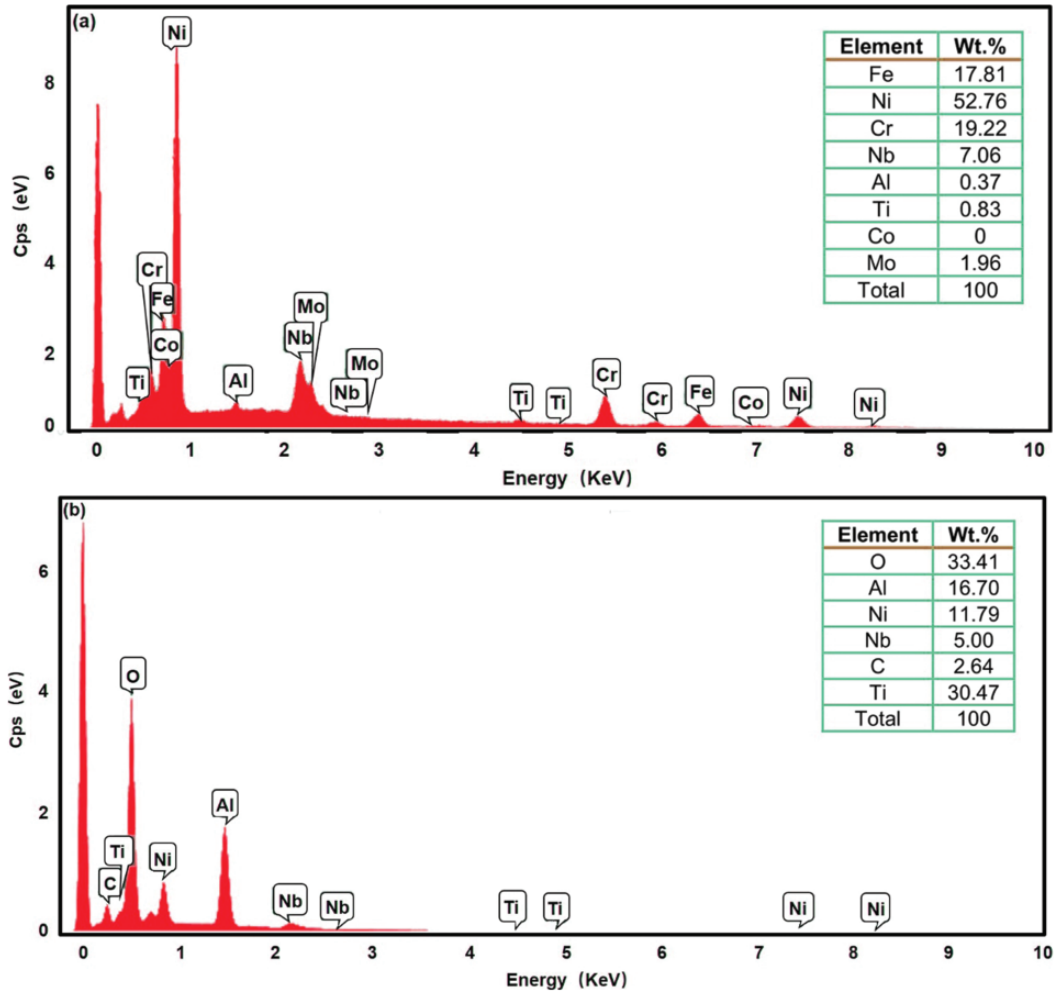

Figure 12: Comparative analysis of chemical compositions: (a) composition of powder reused five times, and (b) composition of spatter particles

point of Ti is also low, at 1660°C. During the SLM process, the spattered particles are sputtered out of the molten pool in the form of an Al-Ti alloy. At the same time, the contents of C and O in the splash particles also increased significantly. The reason behind this effect was that the high-temperature oxidation behavior of the splash particles resulted in the formation of oxides [23], so the oxygen content increased. When the black smoke generated in the process of laser melting powder is not removed by the gas circulation system in time, the content of the element C in the gas atmosphere of the molding cavity is increased, and the content of the element C in the solidified splash particles is thereby increased. The content of Nb even reached 7.06%, exceeding the standard range of 4.75% to 5.5%. The chemical elements in the SLM process will deviate. Therefore, the powder should not be reused too many times.

The above analysis shows that the morphology and content of chemical elements of the splash particles are different from those of fresh powder. Splash particles are larger in size compared to fresh powder. Large splash powders can prevent the complete melting of the powder layer, thereby increasing the possibility of unfusion and pore formation [42], which directly affects the molding quality of SLM parts. Therefore, strict control of powder characteristics including the morphology and size is required [43]. At the same time, it is of great significance to study the influence of splash particles on internal defects of parts.

3.5 Influence of Spatter on the Internal Defects of SLM Parts

To improve the accuracy of the experimental results and avoid the impact of accidental factors, a total of three tests were performed under the same laser energy density. Fig. 13 shows the optical microscopy image and defect distribution of the cross section of a part under different laser energy densities. Three types of defects—micropores, irregular pores, and unfused defect—are mainly observed. It is worth mentioning that this presents a regular internal defect form under the same energy density in Fig. 13. High-energy density laser beams on the molten pool will cause the molten pool to emit high-intensity light, which means that the metal droplets will splash violently, forming a large number of splash particles, and the splashes falling on the powder bed will be mixed into the unfused powder. During the powder-coating process, the splash particles will affect the prefilling of the powder, making the powder unsmooth and forming a gap around the splash particles. During scanning, small sputtered particles can be completely melted, while sputtered particles larger than the preset powder layer thickness can only be partially melted, and the laser cannot reach the vicinity of the sputtering position. At the end of the scan, unmelted splash particles and gaps will form unfused defects, as shown in Figs. 13(a)–13(b). When the energy density is reduced, the light intensity of the molten pool is weakened, and the splashing is not as strong. It can be observed that the interior of the part is mainly irregular pores and micropores, as shown in Figs. 13(c)–13(d).

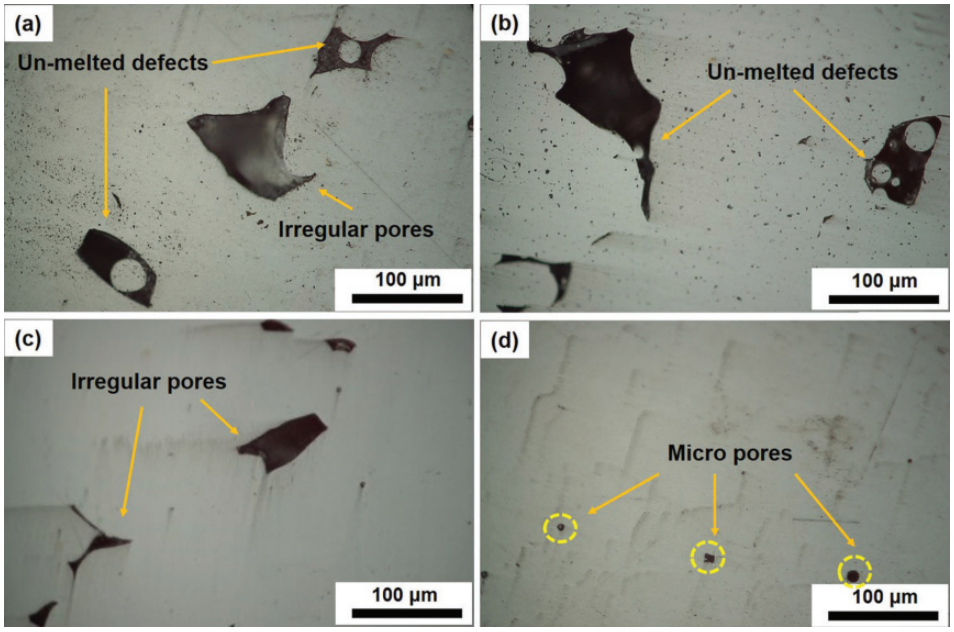

Figure 13: Morphology of the internal defects of SLM parts under different energy densities: (a) 229.17 J/mm^3, (b) 183.33 J/mm^3, (c) 152.78 J/mm^3, and (d) 130.95 J/mm^3

Based on the above analysis, it can be judged that the light intensity of the molten pool depends on the input energy density. The light intensity of the molten pool can explain the intensity of the splash. The splash particles have a direct impact on the internal defects of the part. There is a quantitative correlation between the three. The experimental data of the three groups have certain fluctuations, and the error bars (see Fig. 14) reflect the fluctuation range of the data. As shown in Fig. 14, with the laser energy density as the independent variable, the relative density of the part and the maximum light intensity of the molten pool are the output variables. When the energy density increases, the light intensity of the molten pool increases with a positive correlation. The increasing maximum light intensity of the molten pool reflects the increase in the degree of splashing. In Fig. 14, it can be seen that the relative density is continuously decreasing, indicating that the increase in splashing will increase the internal defects of the part. The relative density is 91.82% when the energy density is 229.17 J/mm^3. As the scanning speed increases, the laser energy density continues to decrease. Under the minimum laser energy density of 130.95 J/mm^3, the densification of the part is the better, with the relative density as high as 99.83%. This shows that although an increase in the scanning speed will lead to a reduction in the energy density, the total sputtering area and the size of the splash particles will also decrease [35]. The laser can still completely melt the powder and the small splash particles. This facilitates the densification process of parts. From the above results, it can be judged that the splash has a negative impact on the structure and performance of the molded part, while increasing the scanning speed (reducing the laser energy density) can improve the formation quality of the part. Studies have shown [44] that in SLM processes, a lower heating intensity reduces spatter generation. Adjusting the laser power, scanning interval and thickness of the powder layer can change the amount of energy input. Therefore, a low-energy density laser beam can be used to melt the metal powder, and then a high-energy density laser beam can be used to remelt it, so that the interlayer bonding is tight and the occurrence of splashes is reduced.

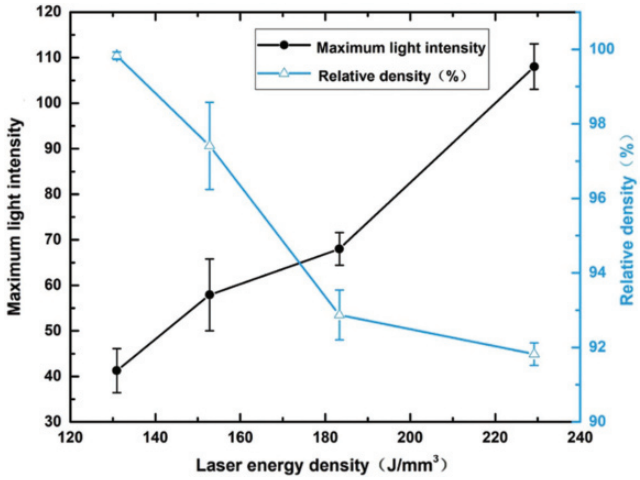

Figure 14: Interrelationships among the energy density, maximum light intensity of the molten pool and relative density

4 Conclusions

In this paper, the transient temperature field of single-channel scanning of IN718 alloy was analyzed by finite element method, and the dynamic behavior of splashing during the SLM processing was observed. The laser intensity changes with different laser energy densities, resulting the continuous change of the light intensity of the formed molten pool. Based on this, the variation law of the light intensity of the molten pool was studied. Furthermore, the formation mechanism, morphology and chemical composition of the

splash particles were analyzed. The correlations between the light intensity of the molten pool, the splash and the internal defects of the part were established. From this, the following conclusions can be drawn:

1. The transient temperature field in the process of laser melting powder changes very dramatically, the powder absorbs energy to form a molten pool quickly, and then the molten pool cools rapidly. Due to the accumulation of heat, the temperature of the molten pool is much higher than the melting point. Furthermore, the molten pool is easy to oscillate and cause splashing, which is consistent with the experimental results. The splash behaviors observed at different shooting frame rates varies greatly. The trail of the splash can be observed at a low shooting frame rate, but the shape and size of the splash cannot be seen. As the shooting frame rate increases, it is easy to observe details such as the morphology, size and quantity of the splash particles, which is conducive to the study and analysis of splash behavior.
2. The light intensity of the molten pool depends on the laser energy input. The greater the energy input, the stronger is the light intensity of the molten pool, which means that the intensity of the splash is greater. The formation process of the spatter is accompanied by continuous changes of the light intensity of the molten pool. At the moment of the splash, the light intensity of the molten pool first increases and then decreases, reaching a peak value at the subthreshold ejection.
3. Compared with fresh powder, the contents of Al and Ti in powder reused 5 times were reduced by 0.15% and 0.02%, respectively. Nevertheless, the two elements in the splash increased significantly, with increases of 16.18% and 29.62%, respectively. The content of Nb even exceeded the standard range. The deviation of chemical elements occurs in the SLM process. Therefore, the powder should not be reused multiple times.
4. Splash particles falling on the powder bed will cause internal voids and unmelted defects in the part. Reducing the laser energy density can reduce the occurrence of splash and improve the formation quality of the part. At a low laser energy density of 130.95 J/mm^3, the densification of the parts is better, with the relative density as high as 99.83%.

Funding Statement: This work was supported by the National Natural Science Foundation of China (Nos. 91860136 and 51801231, Zhou, X., http://www.nsfc.gov.cn/), the Key R & D plan of Guangdong Province (No. 2018B090905001, Zhou, X., http://pro.gdstc.gov.cn/) and the Key Science and Technology project of Shaanxi Province (No. 2018zdzx01-04-01, Zhou, X., http://kjt.shaanxi.gov.cn/).

Conflicts of Interest: The authors declare that they have no conflicts of interest to report regarding the present study.

References

1. Kruth, J. P., Levy, G., Klocke, F., Childs, T. H. C. (2007). Consolidation phenomena in laser and powder-bed based layered manufacturing. *CIRP Annals, 56(2),* 730–759. DOI 10.1016/j.cirp.2007.10.004.
2. Gu, D. D., Meiners, W., Wissenbach, K., Poprawe, R. (2012). Laser additive manufacturing of metallic components: materials, processes and mechanisms. *International Materials Reviews, 57(3),* 133–164. DOI 10.1179/1743280411Y.0000000014.
3. Zhang, B., Dembinski, L., Coddet, C. (2013). The study of the laser parameters and environment variables effect on mechanical properties of high compact parts elaborated by selective laser melting 316L powder. *Materials Science and Engineering: A, 584,* 21–31. DOI 10.1016/j.msea.2013.06.055.
4. Zhang, B., Liao, H., Coddet, C. (2012). Effects of processing parameters on properties of selective laser melting Mg-9% Al powder mixture. *Materials & Design, 34,* 753–758. DOI 10.1016/j.matdes.2011.06.061.
5. Dadbakhsh, S., Hao, L. (2012). Effect of Al alloys on selective laser melting behaviour and microstructure of in situ formed particle reinforced composites. *Journal of Alloys and Compounds, 541,* 328–334. DOI 10.1016/j.jallcom.2012.06.097.

6. Song, B., Dong, S., Coddet, P., Zhou, G., Ouyang, S. et al. (2013). Microstructure and tensile behavior of hybrid nano-micro SiC reinforced iron matrix composites produced by selective laser melting. *Journal of Alloys and Compounds, 579,* 415–421. DOI 10.1016/j.jallcom.2013.06.087.
7. Vrancken, B., Thijs, L., Kruth, J. P., Van Humbeeck, J. (2012). Heat treatment of Ti6Al4V produced by selective laser melting: microstructure and mechanical properties. *Journal of Alloys and Compounds, 541,* 177–185. DOI 10.1016/j.jallcom.2012.07.022.
8. Zhang, B., Fenineche, N. E., Liao, H., Coddet, C. (2013). Microstructure and magnetic properties of Fe-Ni alloy fabricated by selective laser melting Fe/Ni mixed powders. *Journal of Materials Science & Technology, 29(8),* 757–760. DOI 10.1016/j.jmst.2013.05.001.
9. Yadroitsev, I., Smurov, I. (2010). Selective laser melting technology: from the single laser melted track stability to 3D parts of complex shape. *Physics Procedia, 5,* 551–560. DOI 10.1016/j.phpro.2010.08.083.
10. Campbell, I., Bourell, D., Gibson, I. (2012). Additive manufacturing: rapid prototyping comes of age. *Rapid Prototyping Journal, 18(4),* 255–258. DOI 10.1108/13552541211231563.
11. Wang, D., Song, C., Yang, Y., Bai, Y. (2016). Investigation of crystal growth mechanism during selective laser melting and mechanical property characterization of 316L stainless steel parts. *Materials & Design, 100,* 291–299. DOI 10.1016/j.matdes.2016.03.111.
12. Xiao, D. M., Yang, Y. Q., Su, X. B., Wang, D., Luo, Z. Y. (2012). Topology optimization of microstructure and selective laser melting fabrication for metallic biomaterial scaffolds. *Transactions of Nonferrous Metals Society of China, 22(10),* 2554–2561. DOI 10.1016/S1003-6326(11)61500-8.
13. Edwards, P., Ramulu, M. (2014). Fatigue performance evaluation of selective laser melted Ti-6Al–4V. *Materials Science and Engineering: A, 598,* 327–337. DOI 10.1016/j.msea.2014.01.041.
14. Kasperovich, G., Hausmann, J. (2015). Improvement of fatigue resistance and ductility of TiAl6V4 processed by selective laser melting. *Journal of Materials Processing Technology, 220,* 202–214. DOI 10.1016/j.jmatprotec.2015.01.025.
15. Khairallah, S. A., Anderson, A. T., Rubenchik, A., King, W. E. (2016). Laser powder-bed fusion additive manufacturing: Physics of complex melt flow and formation mechanisms of pores, spatter, and denudation zones. *Acta Materialia, 108,* 36–45. DOI 10.1016/j.actamat.2016.02.014.
16. Zhang, P., Zhou, X., Cheng, X., Sun, H., Ma, H. et al. (2019). Elucidation of bubble evolution and defect formation in directed energy deposition based on direct observation. *Additive Manufacturing, 32,* 101026. DOI 10.1016/j.addma.2019.101026.
17. Wang, D., Dou, W., Yang, Y. (2018). Research on selective laser melting of Ti6Al4V: surface morphologies, optimized processing zone, and ductility improvement mechanism. *Metals, 8(7),* 471. DOI 10.3390/met8070471.
18. Wang, D., Yang, Y., Yi, Z., Su, X. (2013). Research on the fabricating quality optimization of the overhanging surface in SLM process. *International Journal of Advanced Manufacturing Technology, 65(9–12),* 1471–1484. DOI 10.1007/s00170-012-4271-4.
19. Wang, D., Liu, Y., Yang, Y., Xiao, D. (2016). Theoretical and experimental study on surface roughness of 316L stainless steel metal parts obtained through selective laser melting. *Rapid Prototyping Journal, 22(4),* 706–716. DOI 10.1108/RPJ-06-2015-0078.
20. Song, C., Zhang, M., Yang, Y., Wang, D., Yu, J. K. (2018). Morphology and properties of CoCrMo parts fabricated by selective laser melting. *Materials Science and Engineering: A, 713,* 206–213. DOI 10.1016/j.msea.2017.12.035.
21. Bai, Y., Yang, Y., Wang, D., Zhang, M. (2017). Influence mechanism of parameters process and mechanical properties evolution mechanism of maraging steel 300 by selective laser melting. *Materials Science and Engineering: A, 703,* 116–123. DOI 10.1016/j.msea.2017.06.033.
22. Chen, L., Li, H., Liu, S., Shen, S., Zhang, T. et al. (2019). Simulation of surface deformation control during selective laser melting of AlSi10Mg powder using an external magnetic field. *AIP Advances, 9(4),* 045012. DOI 10.1063/1.5085735.

23. Jia, Q., Gu, D. (2014). Selective laser melting additive manufactured Inconel 718 superalloy parts: high-temperature oxidation property and its mechanisms. *Optics & Laser Technology, 62,* 161–171. DOI 10.1016/j.optlastec.2014.03.008.
24. Zhang, M. J., Chen, G. Y., Zhou, Y., Li, S. C., Deng, H. (2013). Observation of spatter formation mechanisms in high-power fiber laser welding of thick plate. *Applied Surface Science, 280,* 868–875. DOI 10.1016/j.apsusc.2013.05.081.
25. Zhang, M., Chen, G., Zhou, Y., Li, S. (2013). Direct observation of keyhole characteristics in deep penetration laser welding with a 10 kW fiber laser. *Optics Express, 21(17),* 19997–20004. DOI 10.1364/OE.21.019997.
26. Zhang, M., Chen, G., Zhou, Y., Liao, S. (2014). Optimization of deep penetration laser welding of thick stainless steel with a 10 kW fiber laser. *Materials & Design, 53,* 568–576. DOI 10.1016/j.matdes.2013.06.066.
27. Low, D. K. Y., Li, L., Corfe, A. G. (2001). Characteristics of spatter formation under the effects of different laser parameters during laser drilling. *Journal of Materials Processing Technology, 118(1–3),* 179–186. DOI 10.1016/S0924-0136(01)00910-4.
28. Low, D. K. Y., Li, L., Byrd, P. J. (2003). Spatter prevention during the laser drilling of selected aerospace materials. *Journal of Materials Processing Technology, 139(1–3),* 71–76. DOI 10.1016/S0924-0136(03)00184-5.
29. Low, D. K. Y., Li, L., Byrd, P. J. (2000). The effects of process parameters on spatter deposition in laser percussion drilling. *Optics & Laser Technology, 32(5),* 347–354. DOI 10.1016/S0030-3992(00)00079-7.
30. Liu, Y., Yang, Y., Mai, S., Wang, D., Song, C. (2015). Investigation into spatter behavior during selective laser melting of AISI 316L stainless steel powder. *Materials & Design, 87,* 797–806. DOI 10.1016/j.matdes.2015.08.086.
31. Wang, D., Wu, S., Fu, F., Mai, S., Yang, Y. et al. (2017). Mechanisms and characteristics of spatter generation in SLM processing and its effect on the properties. *Materials & Design, 117,* 121–130. DOI 10.1016/j.matdes.2016.12.060.
32. Wang, D., Ye, G., Dou, W., Zhang, M., Yang, Y. et al. (2020). Influence of spatter particles contamination on densification behavior and tensile properties of CoCrW manufactured by selective laser melting. *Optics & Laser Technology, 121,* 105678. DOI 10.1016/j.optlastec.2019.105678.
33. Simonelli, M., Tuck, C., Aboulkhair, N. T., Maskery, I., Ashcroft, I. et al. (2015). A study on the laser spatter and the oxidation reactions during selective laser melting of 316L stainless steel, Al-Si10-Mg, and Ti-6Al-4V. *Metallurgical and Materials Transactions A, 46(9),* 3842–3851. DOI 10.1007/s11661-015-2882-8.
34. Andani, M. T., Dehghani, R., Karamooz-Ravari, M. R., Mirzaeifar, R., Ni, J. (2017). Spatter formation in selective laser melting process using multi-laser technology. *Materials & Design, 131,* 460–469. DOI 10.1016/j.matdes.2017.06.040.
35. Andani, M. T., Dehghani, R., Karamooz-Ravari, M. R., Mirzaeifar, R., Ni, J. (2018). A study on the effect of energy input on spatter particles creation during selective laser melting process. *Additive Manufacturing, 20,* 33–43. DOI 10.1016/j.addma.2017.12.009.
36. Díaz-álvarez, J., Cantero, J. L., Miguélez, H., Soldani, X. (2014). Numerical analysis of thermomechanical phenomena influencing tool wear in finishing turning of inconel 718. *International Journal of Mechanical Sciences, 82,* 161–169. DOI 10.1016/j.ijmecsci.2014.03.010.
37. Yin, J., Wang, D., Yang, L., Wei, H., Dong, P. et al. (2020). Correlation between forming quality and spatter dynamics in laser powder bed fusion. *Additive Manufacturing, 31,* 100958. DOI 10.1016/j.addma.2019.100958.
38. Andani, M. T., Haberland, C., Walker, J., Elahinia, M. (2014). An investigation of effective process parameters on phase transformation temperature of nitinol manufactured by selective laser melting. *ASME 2014 Conference on Smart Materials, Adaptive Structures and Intelligent Systems, American Society of Mechanical Engineers Digital Collection.*
39. Semak, V., Matsunawa, A. (1997). The role of recoil pressure in energy balance during laser materials processing. *Journal of Physics D: Applied Physics, 30(18),* 2541–2552. DOI 10.1088/0022-3727/30/18/008.
40. Brooks, R. F., Monaghan, B., Barnicoat, A. J., McCabe, A., Mills, K. C. et al. (1996). The physical properties of alloys in the liquid and mushy states. *International Journal of Thermophysics, 17(5),* 1151–1161. DOI 10.1007/BF01442002.

41. Li, S., Chen, G., Katayama, S., Zhang, Y. (2014). Relationship between spatter formation and dynamic molten pool during high-power deep-penetration laser welding. *Applied Surface Science, 303,* 481–488. DOI 10.1016/j.apsusc.2014.03.030.

42. Esmaeilizadeh, R., Ali, U., Keshavarzkermani, A., Mahmoodkhani, Y., Marzbanrad, E. et al. (2019). On the effect of spatter particles distribution on the quality of Hastelloy X parts made by laser powder-bed fusion additive manufacturing. *Journal of Manufacturing Processes, 37,* 11–20. DOI 10.1016/j.jmapro.2018.11.012.

43. Tan, J. H., Wong, W. L. E., Dalgarno, K. W. (2017). An overview of powder granulometry on feedstock and part performance in the selective laser melting process. *Additive Manufacturing, 18,* 228–255. DOI 10.1016/j.addma.2017.10.011.

44. Song, B., Dong, S., Liu, Q., Liao, H., Coddet, C. (2014). Vacuum heat treatment of iron parts produced by selective laser melting: microstructure, residual stress and tensile behavior. *Materials & Design (1980–2015), 54,* 727–733. DOI 10.1016/j.matdes.2013.08.085.